IOP Publishing Plasma Sources Science and Technology
Plasma Sources Sci. Technol. **27** (2018) 055002 (13pp) https://doi.org/10.1088/1361-6595/aabd13

A compact new incoherent Thomson scattering diagnostic for low-temperature plasma studies

Benjamin Vincent[1], **Sedina Tsikata**[1,4], **Stéphane Mazouffre**[1], **Tiberiu Minea**[2] **and Jérôme Fils**[3]

[1] ICARE, CNRS (UPR 3021), 1C ave. de la Recherche Scientifique, F-45071, Orléans, France
[2] LPGP, CNRS (UMR 8578), Université Paris-Sud, Université Paris Saclay, F-91405, Orsay Cedex, France
[3] GSI Helmholtzzentrum für Schwerionenforschung GmbH, Planckstraße 1, D-64291, Darmstadt, Germany

E-mail: benjamin.vincent@cnrs-orleans.fr and sedina.tsikata@cnrs-orleans.fr

Received 19 December 2017, revised 21 March 2018
Accepted for publication 10 April 2018
Published 8 May 2018

Abstract

Incoherent Thomson scattering (ITS) has a long history of application for the determination of electron density and temperature in dense fusion plasmas, and in recent years, has been increasingly extended to studies in low-temperature plasma environments. In this work, the design and preliminary implementation of a new, sensitive and uniquely compact ITS platform known as *Thomson scattering experiments for low temperature ion sources* are described. Measurements have been performed on a hollow cathode plasma source, providing access to electron densities as low as 10^{16} m^{-3} and electron temperatures of a few eV and below. This achievement has been made possible by the implementation of a narrow volume Bragg grating notch filter for the attenuation of stray light, a feature which guarantees compactness and reduced transmission losses in comparison to standard ITS platforms.

Keywords: incoherent Thomson scattering, laser diagnostics, Raman scattering, volume Bragg grating notch filter, hollow cathode plasma

1. Introduction

Improving the understanding of the complex physics of plasma sources, including phenomena such as turbulence and transport, requires access to fundamental measurements of the particle properties. A number of diagnostic tools are available for the determination of electron properties. Electrostatic probes such as Langmuir probes [1, 2] inserted directly into the plasma provide access to electron temperature and density through the measurement of their current–voltage characteristics. However, such tools have certain shortcomings, such as plasma perturbation (due for example to sputtering), and are susceptible to damage in regions of high particle density and temperature. Available probe theories are also inadequate for use in magnetized plasma regions [3] and for high-pressure, collisional plasmas [4]; in such plasmas the required condition for the application of conventional theories—that the electron mean free path greatly exceeds the sheath radius—is not satisfied.

Techniques such as optical emission spectroscopy (OES) [5, 6] and interferometry [7, 8] may also be applied to the determination of electron properties. OES involves the analysis of spectral lines of excited species to obtain information on the electron temperature and electron energy distribution function (EEDF). While simple to implement, it relies on complex collisional-radiative [9, 10] models (requiring highly-accurate knowledge of cross-sections, difficult to obtain for many gases) or corona equilibrium models (which rely on assumptions regarding the concentration of excited states and the nature of the transitions involved).

In interferometry, electron density is determined by relating it to a phase shift occurring when incident radiation traverses a plasma. Like OES, it is a non-invasive, non-perturbative line-of-sight measurement; conventional reflectometry techniques have limitations on the attainable temporal and spatial resolution.

[4] Author to whom any correspondence should be addressed.

Incoherent Thomson scattering (ITS) [11] has been applied for the measurement of electron temperature and density in dense fusion plasmas since the 1960s up to the present day [12–17]. It is a non-invasive, direct and spatially-resolved measurement technique. Applying this technique in low-temperature plasmas is a challenge due to the low plasma densities encountered in such environments (down to 10^{16} m^{-3}), resulting in low scattered signal intensities. While the technique is generally considered non-perturbative, recent work indicates that ponderomotive effects must be taken into account at low plasma densities [18].

Over the last two decades, this technique has been extended to a larger range of plasma sources by several different authors, as seen for instance in [19–25]. These different sources have electron temperatures on the order of a few eV and electron densities ranging from about 10^{16}–10^{21} m^{-3}.

In this work, we describe the design and preliminary implementation of a compact new ITS tool destined for measurements in sources such as Hall thrusters [26], hollow cathodes [27], planar magnetrons [28] and electron cyclotron resonance (ECR) sources [29], among others. The diagnostic is intended to provide measurements in low electron density environments (Hall thrusters: 10^{16}–10^{18} m^{-3}, planar magnetrons: 10^{16}–10^{18} m^{-3} in DC operation, as high as 10^{20} m^{-3} in high-power pulsed operation, ECR sources: 10^{16}–10^{18} m^{-3}). The diagnostic is also intended to provide access to a wide range of electron temperatures (from below 1 eV to several tens of eV in the aforementioned sources), and is destined for electron property measurement in continuous and pulsed operation of these sources.

The planned applications are intended to improve basic physics understanding in the aforementioned sources, required for accurate modeling and source development. In Hall thrusters, for example, probe measurements are not considered reliable in the magnetized near-field region of the plasma. Yet this is a region where fundamental features such as ion acceleration and microturbulence play important roles. The development of a suitable diagnostic for the measurement of electron properties in such regions is considered important to future progress in the field. Indeed, recent attempts have been made to apply ITS to the study of propulsion plasmas [30, 31] and a new cavity-enhanced implementation is also being explored [32].

Electron temperature and density measurements, combined with measurements of electron dynamics, would provide in-depth information which is difficult to obtain in low-temperature plasmas. The new ITS diagnostic is intended for use with another recently-developed, highly-sensitive coherent Thomson scattering diagnostic known as PRAXIS [33]. PRAXIS has been used in recent years for microturbulence studies in low-temperature plasmas of Hall thrusters [33, 34] and planar magnetrons [33]. These works provided the first experimental identifications and characterizations of the electron cyclotron drift instability [35], implicated in anomalous electron transport, in such environments. The combination of the two diagnostics can, for instance, be used to investigate specific aspects such as the role of the instability in electron heating.

Section 2 of this paper presents the main features of the new diagnostic and its key components. The diagnostic calibration and spectrum analysis procedures are outlined in section 3. Section 4 presents Thomson scattering results from the diagnostic experimental implementation on a hollow cathode plasma source (the first of its kind), and conclusions are presented in section 5.

2. Diagnostic description

Thomson scattering is the scattering of incident electromagnetic radiation on free charged particles. The particles are accelerated by the incident radiation and emit, in turn, scattered fields—an effect which is more important for electrons, much lighter than ions. Two scattering regimes [36] involving free electrons are denoted according to a scattering parameter α, with $\alpha = 1/k\lambda_{De}$. k is the observation wavenumber and λ_{De} the electron Debye length. The observation wave vector $\vec{k}$ is defined according to the Bragg relation: $\vec{k} = \vec{k_s} - \vec{k_i}$, where $\vec{k_s}$ and $\vec{k_i}$ are the scattering and incident wave vectors, respectively.

For $\alpha > 1$, the scattering regime is termed collective or coherent: the scattering length scales are greater than than the Debye length, allowing collective electron fluctuations to become visible. For $\alpha \ll 1$, the scattering regime is incoherent. In this case, the scattering length scales are shorter than the electron screening length, allowing individual electron fluctuations to be observed. The scattered intensity in this latter case is the sum of the contributions from the individual electron scatterers. It reflects the electron density (via the total number of scatterers) and temperature (or, more generally, the electron velocity distribution function (EVDF), via the Doppler shift of the frequency of the scattered radiation due to the electron motion). This work focuses on the incoherent scattering regime.

The main features of the diagnostic design are presented in this section. The new diagnostic is named *Thomson scattering experiments for low temperature ion sources* (THETIS). The optical bench is set up according to figure 1. A top view of the bench and its installation for hollow cathode investigations in a vacuum vessel (length 1.8 m, diameter 0.8 m) are shown. The vessel is equipped with primary, turbomolecular and cryogenic pumps to maintain a base pressure of 10^{-7} mbar. The incident laser beam trajectory of the transmission branch is shown in dark green, and the detection branch laser beam trajectory is shown in light green. The plasma volume is indicated in blue.

2.1. Transmission branch

To ensure adequate performance of the transmission branch, (i) a high level of incident radiation is required (while avoiding processes such as photo-ionization and plasma perturbation [37] due to high power densities in the observation volume), (ii) stray light reflections which could obscure the Thomson scattering signal or damage the detector are to be minimized, and (iii) losses at optical elements (mirrors, lenses) are to be minimized.

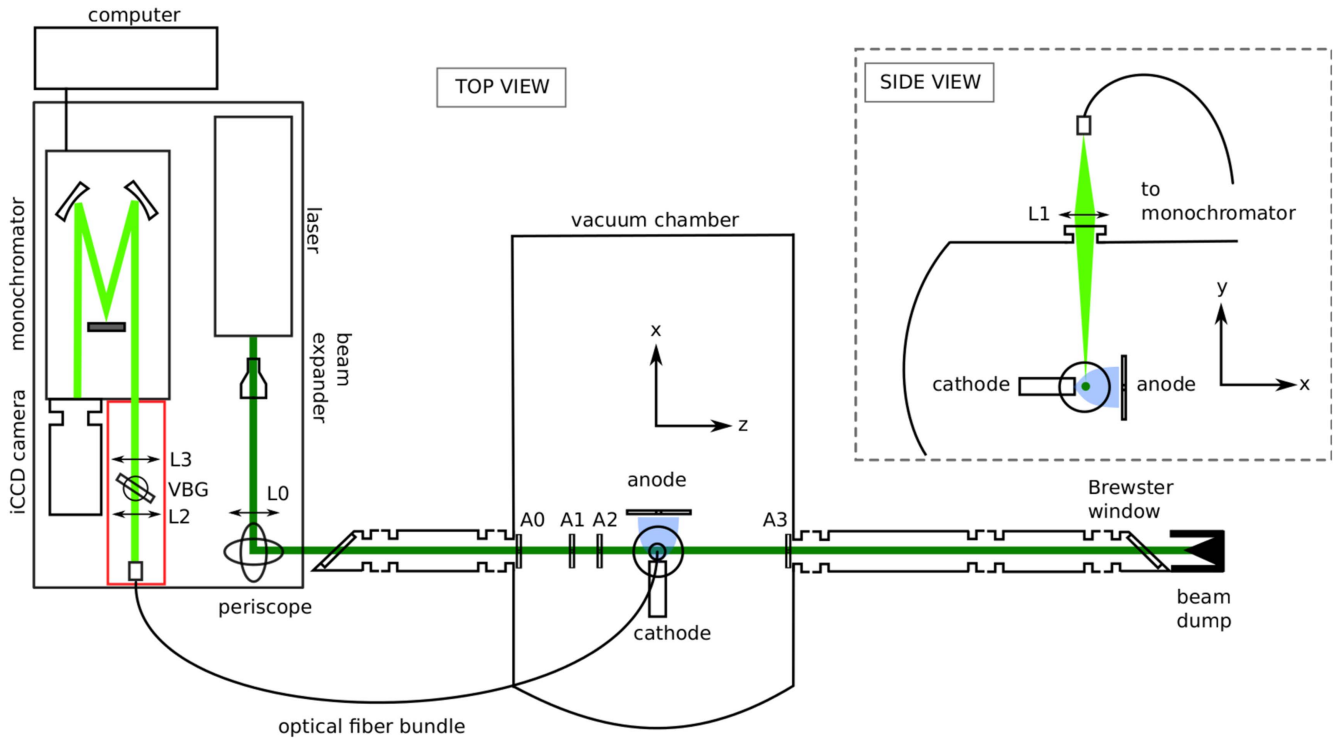

Figure 1. View of the THETIS ITS bench setup (not to scale). Two views are shown: a top view of the bench and laser beam trajectory (in dark green) and a side view, showing the collection of scattered light (in light green) at the top of the vacuum vessel. *L*0, *L*1, *L*2 and *L*3 indicate lenses; *A*0, *A*1, *A*2 and *A*3 indicate apertures; VBG indicates the volume Bragg grating notch filter used for Rayleigh and stray light suppression. The plasma volume is shown in blue.

The transmission branch uses a Quantel Nd:YAG laser (Q-Smart 850) frequency-doubled for operation at 532 nm (with a pulse width of 6 ns, repetition rate of 10 Hz, nominal pulse power of 430 mJ, and a beam diameter at the exit of the laser cavity of 9 mm). This choice of wavelength was made due to the availability of high-efficiency detectors and optics with high transmission at 532 nm. The laser model was chosen for compactness (required in a setup to be implemented on several sources), high pulse power and stability.

The laser beam is first sent to a beam expander which increases the diameter by a factor of 3 (reducing the beam divergence by the same factor). This beam expander is composed of fused silica lenses, coated for a maximum reflectance R of 0.25% at 532 nm. The exiting beam is then transmitted to a fused silica lens $L0$ (50 mm diameter, focal length 2000 mm, $R < 0.25\%$ at 532 nm) for focusing in the observation volume of the plasma. A periscope assembly, using fused silica mirrors coated for a reflectance >99.6% at 532 nm, are used to transmit light to the observation volume.

The entering beam is polarized in the xy plane (with >80% of the incident optical power along the x direction). The vacuum chamber is equipped with custom fused silica Brewster windows (100 mm minor diameter) mounted at the end of aluminum tubes (total lengths 0.8 and 1.3 m in the current implementation). The use of long tubes for the mounting of the Brewster windows ensures that any reflections at the window surfaces have a low probability of reaching the measurement volume.

As seen in figure 1, a number of apertures have been set up between the entering laser beam, starting at the vessel wall and up to the plasma volume, with a last aperture at the second vessel wall. These elements, identified by *A*0, *A*1, *A*2 and *A*3 in figure 1, are intended to further minimize the propagation of stray light (originating from reflections on optical components such as windows). The vessel apertures are constructed from thin metal sheets and diaphragms with matte black coatings. In the center of the plasma volume, the measured beam waist is about 0.3 mm. After traversing the plasma, the beam is sent to a beam dump with a large acceptance aperture (66 mm diameter) which provides multiple internal reflections, limiting the return of dumped light to the plasma.

2.2. Detection branch

Increasing the incident laser power indefinitely to maximize the Thomson scattered intensity is not feasible, due to plasma perturbation at high laser energies. Instead, the detection branch is designed to recover the maximum number of photons by limiting optics losses as much as possible (for example, by reducing the number of mirrors and lenses required to recover the scattered radiation).

Scattered radiation is recovered perpendicular to the incident beam line, in the y direction, as seen in figure 1. Here, a 100 mm diameter fused silica, plano-convex lens $L1$ of 200 mm focal length (coated for $R < 0.25\%$ at 532 nm) placed at the top port of the vacuum vessel is used to recover

the radiation and focus it onto the end of a fiber bundle. In the side view image (inset), the distance between $L1$ and the center of the plasma is 520 mm; the lens and fiber bundle end are separated by 325 mm. This gives an image magnification factor of 0.625.

2.2.1. Fiber bundle. A custom fiber bundle is used to relay light collected from the scattering volume to a spectrometer. This fiber bundle is composed of 45 fused silica fibers (NA $= 0.22 \pm 0.02$) of diameter 300 μm, stacked in a 15 $\times$ 3 matrix on one end and a 45 $\times$ 1 matrix at the other. The use of fiber arrays to collect scattered light has been performed by other authors, for example, in [38]. This method of light collection has some advantages. It is possible to maximize collection of the scattered light while still providing an easily-adjustable spatial resolution of the observation region (obtained by changing the number of collecting fibers). The stacking used for collection (15 $\times$ 3) allows for easy recovery of the scattered light and is robust to misalignment, while the 45 $\times$ 1 configuration at the spectrometer end allows for measurement within a narrow spectrometer slit of 300 μm. The fiber bundle also simplifies the mounting of the detection branch. All of these advantages are important for a diagnostic specifically designed for ready installation on a variety of vacuum chambers and plasma sources.

Light from the scattering volume is focused onto a reduced number of fibers by the lens $L1$. Taking into account the system magnification and the number of fibers imaged (5 $\times$ 3 matrix), the maximum area which can be viewed in the plane zx has dimensions of 2.4 $\times$ 1.4 mm. However, the actual scattering length viewed along x is set by the laser beam waist (0.3 mm). Assuming a scattering length along y also set by the dimensions of the laser beam waist, the plasma scattering volume from which the signal is recorded has dimensions of 0.216 mm^3 (0.3 $\times$ 2.4 $\times$ 0.3 mm). The signal from all 15 imaged fibers is summed to compose the scattered spectrum.

2.2.2. Volume Bragg grating (VBG) notch filter. We have incorporated a unique feature in our Thomson scattering diagnostic: a spectrally-narrow, reflecting, VBG notch filter used to significantly attenuate light at 532 nm (composed of stray light and Rayleigh-scattered light on atoms and molecules). To act as filters, such gratings have modulated refractive indices to allow the selective reflection of light at a particular wavelength and angle of incidence respecting the Bragg condition. Our setup uses such a filter developed by OptiGrate. Figure 2(b) shows attenuation as a function of wavelength for the 532 nm grating used in this work, with a FWHM of only 0.2 nm and a maximum optical density of 4.

Figure 2(a) shows the sensitivity of the grating attenuation to the angle (which is referenced with respect to a perpendicular incidence angle of 0°). The FWHM of this profile is 0.3°; maximizing the attenuation requires limiting the beam divergence below this value.

The filter used is identified by VBG in figure 1 and is placed between lenses $L2$ and $L3$, both of focal length

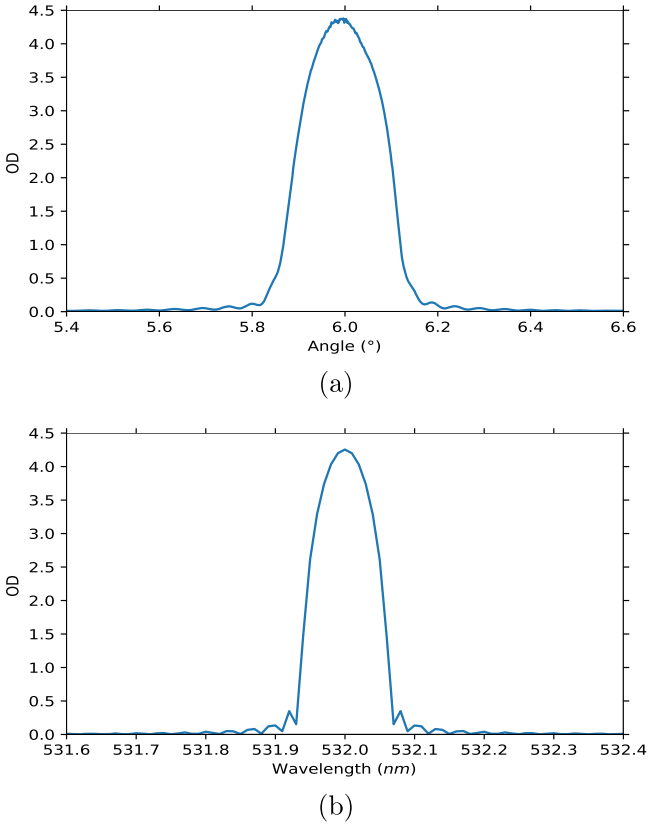

Figure 2. Optical density (OD) of the volume Bragg grating notch filter as a function of incident (a) angle and (b) wavelength (courtesy: OptiGrate).

100 mm and diameter 25.4 mm. The performance of the filter is dependent on limiting the divergence of the incoming beam; the positioning of $L2$ ensures the collimation of the light arriving at the filter. $L3$ focuses the light within the spectrometer's acceptance angle. Adjustment of the orientation of the filter is performed using a micrometric rotation stage on which it is mounted.

In recent years, filters of this type have been successfully used by other teams for Raman scattering experiments [39, 40]. To our knowledge, this is the first implementation of the VBG notch filter for a Thomson scattering application. The use of a single spectrometer paired with a VBG notch filter limits the number of mirrors used in the detection branch (reducing potential losses), and the transmission efficiency of the VBG notch filter itself, outside the narrow bandstop region (≈0.3 nm), exceeds 96%. For a standard, high-efficiency triple grating spectrometer (even with coatings for the UV–vis range), transmission efficiency is on the order of 15%. The compactness of our setup can be attributed to the replacement of a triple grating spectrometer by the single grating spectrometer paired with the VBG notch filter. Our optical bench has dimensions of only 1.5 $\times$ 0.75 m; a typical triple grating spectrometer alone could occupy a similar area.

In our setup, we are presently limited to a VBG with a clear aperture of 11 $\times$ 11 mm, for reasons of cost at the time of mounting of our prototype; this limitation results in the loss

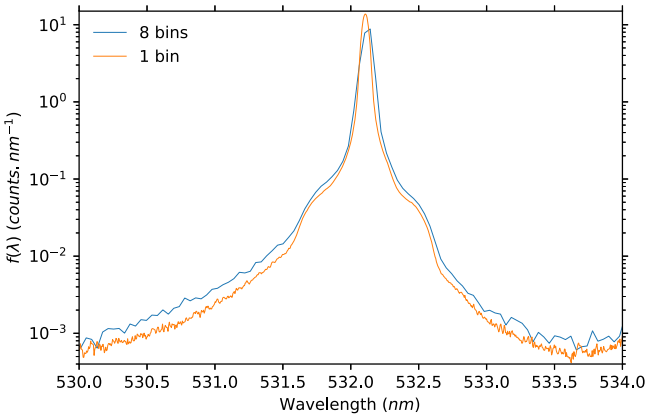

Figure 3. Instrument function profile for the THETIS diagnostic with a 300 μm spectrometer slit width, without horizontal wavelength binning and with binning over eight horizontal pixels.

of some radiation which falls outside the filter dimensions. This point is discussed further in section 4.6.

2.2.3. Spectrometer and camera. This setup uses a single spectrometer. The spectrometer (a Princeton Instruments Acton SP-2750, f/9.7) is fitted with silver-coated mirrors (reflectivity in the visible spectrum range >98%). It uses one of two turret-mounted gratings: a ruled grating (600 lines mm^{-1}), or a blazed holographic grating (2400 lines mm^{-1}). These gratings allow us to select between covering the spectral width expected at high temperatures (tens of eV) and providing adequate wavelength resolution at low electron temperatures (a few eV).

The detector is a Princeton Instruments ICCD PI-MAX 4-1024f camera, triggered using the laser Q-switch signal. Its Gen II intensifier has a quantum efficiency of 10% at 532 nm. The front-illuminated CCD dimensions are 13.3 × 13.3 mm (with pixels of size 13 × 13 μm).

The combined spectrometer and camera features provide a full wavelength coverage, determined at 532 nm, of 5.1 nm and 28.6 nm, respectively, for the 2400 lines mm^{-1} and 600 lines mm^{-1} grating. The wavelength coverage can be expressed in terms of a corresponding electron velocity and energy coverage,

$$v = \frac{c\Delta\lambda}{2\lambda_i \sin\left(\frac{\theta}{2}\right)} \tag{1}$$

and

$$E = \frac{1}{2} m_e v^2, \tag{2}$$

where v is an equivalent velocity (based on a spectral half-shift $\Delta\lambda$) and E is the corresponding energy associated with this velocity. m_e, λ_i and θ are the electron mass, incident laser wavelength and scattering angle, respectively. These expressions give a v of 1.0 × 10^6 m s^{-1} and 5.7 × 10^6 m s^{-1} for the 2400 lines mm^{-1} and 600 lines mm^{-1} gratings, respectively. The corresponding energy coverage (half-spectrum) is 2.94 and 92.3 eV, respectively.

With the minimum slit width of the spectrometer (highest resolution), the narrowest signal is 3 pixels wide. This corresponds to a maximum resolution of 0.09 nm for the 600 lines mm^{-1} grating and 0.018 nm for the 2400 lines mm^{-1} grating.

The camera and spectrometer are controlled simultaneously using the same Princeton Instruments LightField program, which allows for the choice of grating, acquisition parameters (such as triggering, detector gain, acquisition duration, pixel binning) and the storing of the acquired spectra. Nanosecond gated operation of the camera is applied; this contributes to the attenuation of light at 532 nm by limiting the collection of stray light from optics far from the observation volume, and by limiting the accumulation of the plasma emission.

3. Spectrum analysis procedures

The use of the ITS diagnostic requires appropriate calibration to determine the absolute electron density, using either Rayleigh scattering or Raman scattering (the electron temperature determination is not dependent on this calibration).

An electromagnetic field incident on an atom or molecule induces an oscillating dipole, and the nature of energy re-emission determines the type of scattering. For atoms or molecules at rest with energy re-emission at the same frequency as the incident radiation, the scattering is of the (elastic) Rayleigh type. On the other hand, if energy absorption causes a change of the vibrational or rotational state of the molecule, scattering is of the (inelastic) Raman type. Resonance Raman scattering is associated with changes in the electronic state of the molecule.

In Raman scattering, the molecule may emit photons of lower energy than the incident photon, in which case the corresponding emission lines (known as Stokes lines) are at wavelengths higher than the incident wavelength. On the other hand, the molecule, if previously in an excited state, may emit photons of higher energies than the incident photons, resulting in spectral emission lines (known as anti-Stokes lines) at shorter wavelengths than the incident radiation.

3.1. Instrument function characterization

Prior to the diagnostic calibration, it is necessary to determine the instrument function of the detection branch under the same acquisition parameters and configuration as those to be used for the calibration and Thomson spectra.

The instrument function is determined according to the following procedure. The vacuum vessel is pumped down to its lowest pressure to remove residual gas (which could contribute to Raman or Rayleigh scattering) and the laser beam is sent across the vessel to provide an artificially-large level of stray light at 532 nm (for example, by allowing the beam to graze a reflective object). This signal is collected by the detection branch. A similar measurement is then made with the laser off, for the same duration; this constitutes the

background noise. The instrument profile is determined from the difference between these two spectra.

The instrument function profile is normalized such that $\Sigma I(\lambda)\delta\lambda = 1$, where $I(\lambda)$ is the intensity (in photodetector counts) and $\delta\lambda$ is the spectral width associated with each pixel. This normalized instrument function will be later convolved with theoretical calibration spectra to account for the actual redistribution of the monochromatic light intensity over the pixels. Such a redistribution is a consequence of the specific features of the detection branch. Since the spectral width of the monochromatic light is negligible in comparison to the instrument function width, it is therefore considered to be a Dirac distribution in its convolution with the instrument function. This redistribution is assumed to be constant over the spectral interval probed.

Figure 3 shows the normalized instrument functions determined for the usual experimental slit width (300 μm) for two cases: in the absence of horizontal pixel binning, and with binning over eight horizontal pixels. With no binning, the FWHM of the instrument function peak is 0.06 nm; with binning over eight pixels, the instrument function FWHM is 0.12 nm.

3.2. Raman analysis for calibration

Rayleigh or Raman scattering are commonly used for the calibration of this diagnostic. For Rayleigh calibration, used for example in [41, 42], the Rayleigh scattered signal and the diagnostic stray light are superposed at the initial laser wavelength. A certain degree of care is required in the use of Rayleigh signals for calibration. Since the detector response is not usually perfectly linear with light intensity (a feature we have observed in our case, with deviations increasing at very high light intensities), there is a risk of inaccuracy when high-amplitude Rayleigh spectra are used to calibrate the weaker Thomson scattered radiation. It is also worth noting that for our particular setup, even at pressures which are expected to give Rayleigh scattering peak amplitudes similar to those of the Thomson scattering signal, the stray light contribution still dominates at 532 nm and this would render our calibrations using this method unreliable. Lastly, the Rayleigh calibration and Thomson spectrum setups differ slightly in their optical components (obtaining the Rayleigh spectrum requires the removal of the Bragg volume grating used to attenuate light at the incident wavelength); such differences between the setups must be taken into account for correct calibration and add another source of uncertainty to the measurement.

In this work, we have opted to use Raman scattering for calibration. The Raman calibration procedure, used for example in [20, 43–45], relies on fitting to rotational emission lines which are shifted with respect to the laser wavelength. We use Raman signals measured at pressures which give spectra of comparable amplitudes to the Thomson scattering spectra.

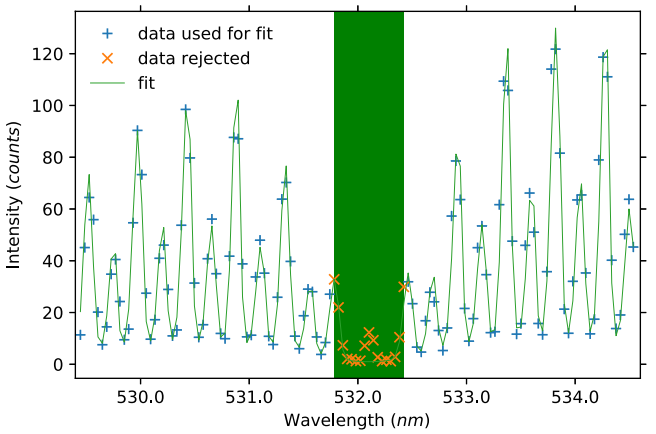

Figure 4. Raman scattering spectrum used for calibration, obtained with nitrogen at 10 mbar and a spectrometer slit width of 300 μm. The green bar at the center of the spectrum shows the region in which points are excluded from the fit.

3.2.1. Raman signal measurement. The following procedure is used to obtain a typical Raman spectrum used for calibration in this work.

The vacuum vessel is filled with nitrogen to a known pressure (10 mbar) and the Bragg volume grating is initially misaligned to allow the detection of a large Rayleigh signal. This Rayleigh signal is used simply for a preliminary alignment of the detection branch, ensuring the correct positioning of the optical fiber used to collect light. Once this alignment is completed, the Bragg grating is realigned to minimize the light peak at 532 nm.

A signal acquisition is performed with the laser beam (repetition frequency 10 Hz) traversing the vessel for 10 min (camera acquisition 6000 exposures/frame), followed by a noise spectrum acquisition with the laser off. This latter signal is subtracted from the first. The use of software binning of eight pixels on the horizontal (wavelength) axis improves the signal to noise ratio by a maximum value of $\sqrt{8}$ compared to the unbinned case.

In this work, we perform signal averaging over each laser shot, rather than simple summation (known as *on-CCD accumulation*). This is because, for our particular acquisition conditions (number of bins, laser repetition rate, gain, etc), the dark current noise in the case of summed records would be larger than the read noise, effectively reducing the final signal to noise ratio.

The Raman spectrum obtained is shown in figure 4. Figure 4 shows the experimental points (blue crosses, orange line) as well as the fit (green line, obtained after the fitting procedure described in section 3.2.3). The blue crosses indicate data points taken into account for fitting, while the orange line passes through all the data points, including points around the laser wavelength which are excluded in fitting.

This figure illustrates the performance of the VBG in attenuating the light at 532 nm, while permitting the Stokes transitions (wavelengths above 532 nm) and anti-Stokes transitions (wavelengths below 532 nm) close to the laser wavelength to be fully resolvable. We have performed similar

Raman spectrum measurements over a range of pressures (0.5–10 mbar) and verified that, with the same value of fit parameters applied to all spectra, superposition of the experimental and theoretical curves scales only with the pressure. This validates the linearity of our detection in this dynamic range and thus, the use of such spectra in calibrations.

3.2.2. Raman spectrum distribution. The spectral peaks seen in figure 4 correspond to transitions from one rotational state to another, with these states characterized by the rotational quantum number J. Only J to $J \pm 2$ transitions are authorized ($J \in \mathbb{N}$). The expected wavelengths and line powers associated with these transitions can be predicted using analytical expressions developed in detail in other works, such as in [46]. Here we summarize only a few useful forms.

The wavelengths of the different Raman peaks associated with these transitions are given by:

$$\lambda_{J\to J+2} = \lambda_i + \frac{\lambda_i^2}{hc} B(4J + 6) \tag{3}$$

for Stokes transitions occurring at shorter wavelengths than λ_i, the initial laser wavelength, and

$$\lambda_{J\to J-2} = \lambda_i - \frac{\lambda_i^2}{hc} B(4J - 2) \tag{4}$$

for anti-Stokes transitions. The constant B is the rotational constant (2.48×10^{-4} eV for N_2) [47].

The distribution of the scattered Raman powers over the various wavelengths is written

$$\frac{\mathrm{d}P_R}{\mathrm{d}\Omega}(\lambda) = n_g P_i L \sum_{J,J'} \frac{n_J(T)}{n_g} \frac{\mathrm{d}\sigma_{R,J\to J'}}{\mathrm{d}\Omega} \delta(\lambda - \lambda_{J\to J'}), \tag{5}$$

where $\delta(\lambda - \lambda_{J\to J'})$ is the Dirac distribution. n_g is the gas density, P_i the incident laser power and L the length of the scattering volume. $\frac{\mathrm{d}\sigma_{R,J\to J'}}{\mathrm{d}\Omega}$ is the differential cross-section for a Raman transition $J \to J'$. n_J represents the density of an initial rotational state J. Equation (5) neglects natural line broadening and pressure broadening (i.e. Stark, impact and collision effects) because the measured Raman peak widths are set by the instrument distortion (determined by the instrument function) which has the more significant contribution.

In equation (5), $\frac{\mathrm{d}\sigma_{R,J\to J'}}{\mathrm{d}\Omega}$ is dependent on the direction of observation, the anisotropy of the molecular polarisability tensor (known as γ), the wavelength $\lambda_{J\to J'}$ associated with a transition, and Placzek–Teller coefficients (known as $b_{J\to J'}$) associated with a transition [47]. We note here that a correct interpolation of γ^2 using the values from [47] gives a value of 0.505×10^{-48} cm^6, different from the value used in some other references. The term n_J respects Maxwell–Boltzmann statistics and is dependent on a partition sum term Q (dependent on the gas temperature T and known rotational gas constant B) and a statistical weighting factor g_J [47].

3.2.3. Raman signal fitting. The expression for the actual measured Raman signal I_{RM} takes into account certain effects: (i) the observation of light within a specific solid angle $\Delta\Omega$, (ii) the transmission τ of the system, representing the fraction of scattered light which is detected following the total optical losses associated with the detection branch and detector conversion efficiency, (iii) the redistribution of the radiation due to the instrument function $I(\lambda)$, and (iv) the discrete nature of the measured signal (due to recording by individual pixels). Taking these features into account, the measured Raman scattering spectrum may be written as

$$I_{\mathrm{RM}}(c_1, \lambda, T) = c_1 n_g P_i \delta\lambda \times \sum_{J,J'} \frac{n_J(T)}{n_g} \frac{\mathrm{d}\sigma_{R,J\to J'}}{\mathrm{d}\Omega} I(\lambda - \lambda_{J\to J'}), \tag{6}$$

where $\delta\lambda$ is the wavelength step associated with one pixel. This function is fitted to the experimental data using a least-squares fitting algorithm to extract an optimized constant, $c_1 = \tau L\, \Delta\Omega$, and T. The values of gas density n_g, laser power P_i and $\delta\lambda$ are entered directly into equation (6). c_1 is considered to be constant over the duration of a measurement campaign. We note that our data analysis involves fitting of the Raman profile, however, some other authors opt for calibration using the area under the Raman profile; either approach is valid.

3.3. Thomson spectral analysis

The total Thomson scattered spectrum power may be expressed generally as

$$\frac{\mathrm{d}P_T}{\mathrm{d}\Omega}(\lambda) = n_e P_i L \frac{\mathrm{d}\sigma_T}{\mathrm{d}\Omega} \frac{1}{\Delta\lambda_g \sqrt{2\pi}} \mathrm{e}^{-\frac{(\lambda-\lambda_0)^2}{2\Delta\lambda_g^2}} \mathrm{d}\lambda, \tag{7}$$

where n_e is the electron density and $\frac{\mathrm{d}\sigma_T}{\mathrm{d}\Omega}$ is the Thomson scattering differential cross-section. The last term is the form factor for a Gaussian distribution of electron energies, with a Gaussian half-width (standard deviation) of $\Delta\lambda_g$ and a central wavelength of λ_0.

The actual measured Thomson spectrum I_{T} is given by

$$I_{\mathrm{T}}(\lambda, \Delta\lambda_g, \lambda_0, n_e) = c_1 n_e P_i \delta\lambda \frac{\mathrm{d}\sigma_{\mathrm{T}}}{\mathrm{d}\Omega} \times \int_{-\infty}^{+\infty} \frac{1}{\Delta\lambda_g \sqrt{2\pi}} \mathrm{e}^{-\frac{(u-\lambda_0)^2}{2\Delta\lambda_g^2}} \cdot I(\lambda - u)\mathrm{d}u. \tag{8}$$

This analytical form contains the parameter c_1 (now known, determined from the Raman fit). The laser P_i is remeasured and is treated as an input term in equation (8), in order to account for possible variations in its value between the Raman and Thomson measurements. The term $\delta\lambda$ is also entered directly.

Thus, the fit of this analytical form to the experimental Thomson spectrum gives the values of n_e, $\Delta\lambda_g$ and λ_0 directly as optimization parameters.

The electron temperature for the data, T_e (again assuming a Maxwellian distribution of the electron velocity) is proportional to the square of Gaussian spectrum width $\Delta\lambda_g$. T_e is

obtained through the following formula:

$$T_e = \frac{m_e c^2}{8k_B \sin^2\left(\frac{\theta}{2}\right)}\left(\frac{\Delta\lambda_g}{\lambda_i}\right)^2, \quad (9)$$

where k_B is Boltzmann's constant, c the light speed in a vacuum and θ the scattering angle (90° in our case).

λ_0 provides an absolute measurement of the wavelength shift associated with the global electron drift; in the absence of a significant global electron velocity, $\lambda_0 = \lambda_i$. In the application of the fit to the experimental data, care is taken to exclude the central portion of the spectrum affected by the presence of the Bragg filter (typically within a range of ± 0.25 nm around λ_i).

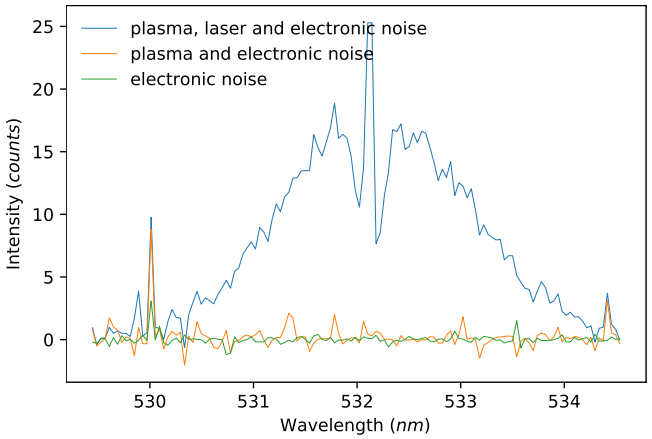

Figure 5. Example of record types made for a typical acquisition (hollow cathode operation at 8 sccm, 2 A).

4. Diagnostic preliminary implementation

4.1. Motivation for hollow cathode investigations

In order to validate the component choices and the diagnostic design, preliminary measurements were designed to measure electron properties of a hollow cathode source [48]. As mentioned in the introduction, the new diagnostic will be applied to investigations of various low pressure magnetized plasma sources, such as Hall thrusters. These are electric propulsion devices whose operation relies on certain fundamental aspects, including (i) the creation of a region of magnetized, energetic electrons for neutral gas ionization and the maintenance of a localized electric field for ion acceleration, and (ii) the neutralization of the accelerated ions. These aspects require an electron source (to feed the ionization region and for recombination with ions). The hollow cathode fulfills these functions and is therefore a critical component in such sources.

The hollow cathode was selected for the first tests for a number of reasons. Firstly, it is simple, compact (the hollow cathode under study has a length of 15 cm) and offers the possibility of full access to the expanding plasma outside the device. Secondly, the expected electron densities (ranging from 10^{16} to 10^{18} m^{-3} for the plasma expanding outside the hollow cathode orifice [49]) are similar to those expected in the sources for which the diagnostic has been designed. Tests on the hollow cathode therefore serve to validate future applications of the diagnostic. Lastly, research into hollow cathodes has undergone a resurgence in recent years, due to attempts to develop hollow cathodes suitable for emerging thruster models [50, 51]. Our preliminary tests, briefly discussed in this work, represent the first time the electron temperatures and densities in hollow cathodes have been measured by ITS.

4.2. Device description

The hollow cathode studied is a device with a 3 mm orifice, operated with xenon gas, and similar to the hollow cathode developed by the Russian MIREA laboratory [52]. It uses a thermo-emissive LaB_6 disc heated by a filament. Emitted electrons ionize the input gas and the maintenance of a sheath close to the emissive disc produces a strong electric field which further increases emission and ionization. An electric field applied between the heater and the anode results in the acceleration of electrons outside the device. In figure 1, the anode (a metal plate) is positioned 40 mm from the hollow cathode orifice; under such conditions the hollow cathode is said to be operating in diode mode. In standard operation of the hollow cathode with a thruster, the anode is situated at the rear of the thruster channel. Nominal operating parameters of this device are a discharge current of 5 A and a gas flow rate of 4 sccm. During experiments the vacuum vessel operating pressure is typically 2–4 $\times$ 10^{-5} mbar. Figure 1 shows the setup for hollow cathode experiments, in which the position of the laser line is maintained and the hollow cathode translated in the x direction for axial investigations of the electron properties.

Hollow cathode operation is known to be characterized by two modes: the 'spot' and 'plume' modes [27]. The spectra shown in this work focus on the spot mode, with higher density and lower-amplitude discharge current oscillations than the plume mode. Experiments are carried out with the same parameters described earlier in the Raman calibration procedure.

4.3. Thomson scattering experiments

4.3.1. Identification of the spectral contributions. Acquisitions of the Thomson scattering signals involve the following records: (i) record *A*—made with both the plasma and laser on, (ii) record *B*—made with the plasma on and the laser off, and (iii) record *C*—made with both the plasma and the laser off.

Figure 5 shows examples of these records for the hollow cathode operating at 8 sccm flow rate and 2 A discharge current. The BVG notch filter is responsible for the attenuation of the 532 nm laser line. Acquisitions have been performed with laser pulse energy (nominal) of 430 mJ, fluence of 6.08 $\times$ 10^6 J m^{-2}, and using averaging over 6000 laser shots (corresponding to a 10 min acquisition duration). The same parameters apply to all subsequent figures.

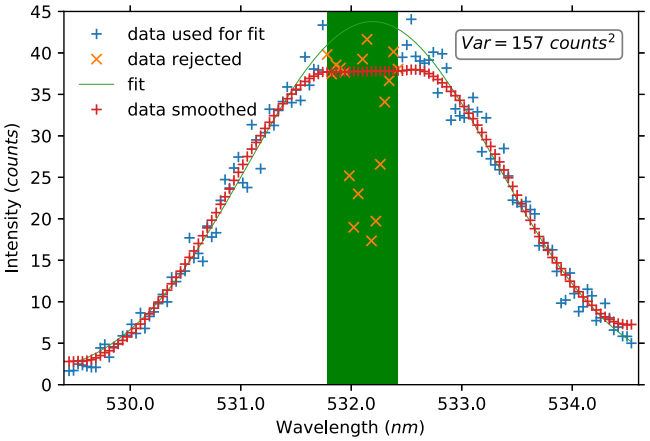

Figure 6. Thomson scattering spectrum obtained for a Xe plasma at 1.3 mm from a hollow cathode orifice, for 16 A discharge current and 8 sccm gas flow rate (spot mode).

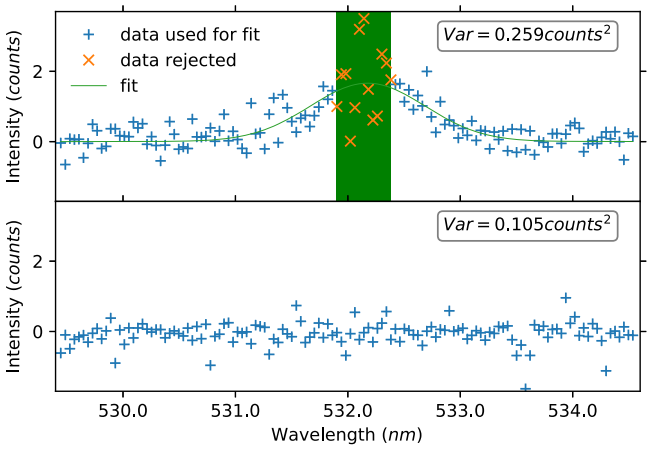

Figure 7. Thomson scattering spectrum obtained for a Xe plasma at 8 mm from a hollow cathode orifice, for 2 A discharge current and 8 sccm gas flow rate (spot mode). The top figure shows the Thomson spectrum and the bottom figure the corresponding noise spectrum.

In figure 5, the electronic noise (shown by the green line) is obtained from the difference between two successive *C* records. The orange curve shows record *B* minus record *C*, and the blue curve shows record *A* minus record *C*. The orange and green curves show similar amplitudes across the wavelength range. This shows that the plasma emission within the camera gating time (15 ns) is not significant enough to present a problem for the measurement (although some low-amplitude emission lines can be discerned in the orange curve, for example, at 530 nm). For the spectra that follow, it is sufficient to subtract record *B* from record *A* to obtain the Thomson scattering signal.

4.3.2. Diagnostic capabilities. Two examples (high and low scattered signal amplitudes) have been chosen to illustrate typical results and signal analysis methods for the Thomson scattering measurements obtained on the hollow cathode. The laser energy, fluence and number of shots are identical to those given for figure 5.

Figures 6 and 7 show, respectively, the Thomson scattering spectra obtained for two operating points for the hollow cathode: (i) at 16 A discharge current and 8 sccm (spot mode) at an axial position 1.3 mm from the hollow cathode orifice, and (ii) at 2 A, 8 sccm (spot mode) at 8 mm from the hollow cathode orifice. As before, the blue crosses and orange line show the experimental data, and the green rectangle shows the spectral region excluded in the curve fitting.

Figure 6 shows the Thomson scattering spectrum obtained from the difference between records *A* and *C*. A Gaussian fit to this data gives values of electron temperature and density of, respectively, 2.27 ± 0.18 eV and $9.41 \pm 0.75 \times 10^{17}$ m^{-3}. The value of Var shown on the figure is the square of the signal standard deviation, calculated over all the points used for the fit (in units of counts^2), which can be regarded as a measurement of the signal power.

Figure 7 shows a noisier signal (with much lower variance) with a Gaussian fit. The figure shows the Thomson signal, obtained from the difference between records *A* and *C* (top) and the corresponding background noise signal, obtained from the difference between records *B* and *C* (bottom). For figure 7, the corresponding values of electron temperature and density are, respectively, 0.46 ± 0.05 eV and $1.8 \pm 0.2 \times 10^{16}$ m^{-3}. The ratio of the Var values of the Thomson signal and background noise in figure 7 provides an idea of the diagnostic sensitivity. For the given acquisition parameters and for Var (Thomson)/Var (noise) = 2.5, the measured electron density is on the order of 10^{16} m^{-3} for an electron temperature below 1 eV.

On the basis of these results, a number of comments may be made:

(i) Even for measurements close to the metallic hollow cathode orifice (figure 6), the attenuation provided by the Bragg volume grating is satisfactory. We note that with the grating absent for the same experimental conditions, we observe saturation of the detector due to a large stray light peak at 532 nm (with saturation corresponding to 65 000 counts). This stray light level drops to 40 counts with the filter present. This is an attenuation of at least a factor of 10^3.

(ii) The narrowness of the bandstop region makes the resolution of low electron temperatures (below 0.5 eV) possible, as seen for the data corresponding to figure 7.

(iii) The low densities measurable, for example, for signals such as that shown in figure 7, are on the same order as those measurable using the most sensitive diagnostics currently available (capable of resolving densities down to 10^{16} m^{-3}). In these preliminary measurements, the acquisition duration has been limited to 10 min, however, the signal to noise ratio can be further improved by increasing the number of horizontal pixels binned, or by increasing the acquisition duration. In section 4.6, avenues for improving the diagnostic sensitivity further are summarized.

(iv) For figure 6, measurements have been performed at a shortest distance of 1.3 mm between the probing laser beam and the hollow cathode orifice, and electron temperatures on the order of a few eV are on the same

order as those expected for this hollow cathode in numerical simulations [49].

(v) Density and temperature measurements correspond to observations made along a particular observation wave vector ($\vec{k}$) direction (determined by the direction of the incident laser crossing the observation volume, and the direction of light collection). To validate any assumption of isotropy, measurements would be required with the observation wave vector oriented in a range of directions at the same measurement position.

(vi) The signal acquisition covers several periods of the kHz-frequency discharge current oscillations. The measured electron properties are thus averaged over these oscillations. We have measured discharge current fluctuations in the spot mode of the hollow cathode of only 2% (discharge current standard deviation/mean discharge current) and expect the measured electron properties to vary little over a discharge current period. However, other sources such as the Hall thruster show discharge current fluctuations of up to 100% in certain regimes, and for investigations on these devices, time resolution of the electron properties will be critical. This may be achieved by (i) first stabilizing the discharge current oscillations to have a well-defined period, and (ii) triggering the signal acquisitions at fixed points in the phase of these stabilized oscillations [53].

4.3.3. Derivation of the electron velocity and energy distribution functions. A Maxwellian distribution of electron velocities leads to a Gaussian scattered spectrum shape, which is commonly characterized with a single electron temperature. However, non-Maxwellian distributions cannot be characterized in the same way. Instead, the use of the EVDF (or EEDF) provides more complete information on the spread in electron energies arising, for example, due to particle heating by plasma turbulence (producing high-energy tails of the distribution functions), the existence of high energy particle beams, or energy losses (resulting in truncated distribution functions). In future implementations of the diagnostic on other sources, we intend to focus on studying such deviations, as has been initiated in certain studies [54, 55]. In this section, we describe the procedures used to determine the EVDF and EEDF. We subsequently determine the EEDF for the data presented in figure 6.

The wavelength shift $\Delta\lambda$ corresponding to a velocity shift v can be expressed as spread in electron energies (using equation (2)). The normalized EVDF along the observation wave vector direction can be obtained from the scattering spectrum with the following expression:

$$f(v) = -\frac{\frac{\mathrm{d}I}{\mathrm{d}\lambda}\Delta\lambda}{\Sigma\left(\frac{\mathrm{d}I}{\mathrm{d}\lambda}\Delta\lambda\delta v\right)}, \tag{10}$$

where δv is the velocity shift associated with the wavelength step ($\delta\lambda$) corresponding to one pixel and $\frac{\mathrm{d}I}{\mathrm{d}\lambda}$ is the derivative of the Thomson-scattered spectral intensity $I(\lambda)$ with respect to λ. The experimental data of the Thomson scattered spectrum are smoothed using a Savitzky–Golay algorithm, which also outputs the derivative $\frac{\mathrm{d}I}{\mathrm{d}\lambda}$.

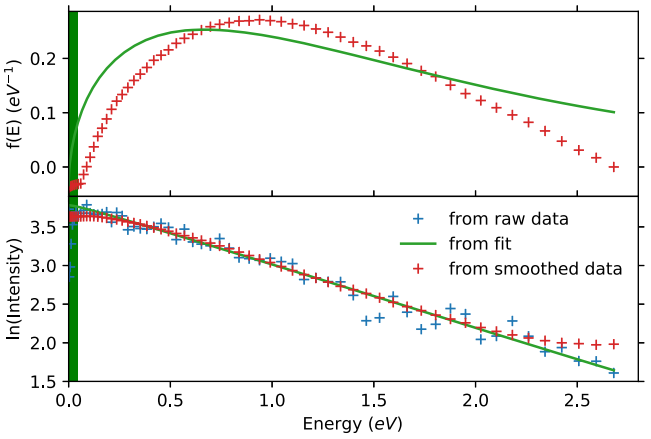

Figure 8. Electron energy distribution function (EEDF) for data shown in figure 6 ($\lambda > \lambda_i$), according to two representations. The smoothed experimental data is shown with red crosses; the green line shows a theoretical EVDF based on a Gaussian spectrum with fit parameters from figure 6. Blue crosses (bottom panel) show the unsmoothed experimental data.

Similarly, the spread in electron energies may be shown using the EEDF (via the relation for the energy shift shown in equation (2)). The normalized EEDF $f(E)$ can be obtained from the scattering spectrum as:

$$f(E) = -\frac{\frac{\mathrm{d}I}{\mathrm{d}\lambda}\mathrm{sgn}(\Delta\lambda)}{\Sigma\left(\frac{\mathrm{d}I}{\mathrm{d}\lambda}\delta E\right)}, \tag{11}$$

where δE is the energy step associated with a single pixel. sgn refers to the mathematical sign function. These forms are based on the more general forms described in [56].

We provide two representations in figure 8 for the spread in electron energies, in order to allow possible deviations from a Maxwellian distribution of electron velocities to become visible. The data shown concerns the side of the Thomson spectrum of figure 6 for which $\lambda > \lambda_i$.

For both panels of figure 8, the red crosses depict the smoothed data and the green line the theoretical curve based on a Gaussian spectrum with the same parameters as figure 6. For both top and bottom panels, the green bar on the right hand side of the figures shows the region excluded due to the presence of the VBG notch filter.

The top panel of figure 8 depicts the classic EEDF. In this panel the area under the red crosses and the green curve is the same over the energy range considered. We note that the form expected for the EEDF, in the case of a Maxwellian velocity distribution, is a chi-squared distribution. The location of the peak for the theoretical curve is shifted with respect to the peak seen for the red crosses; this is due simply to the slight difference in the point of inflection for the fit curve and for the smoothed data seen in figure 6. This slight difference is magnified in this representation, due to the derivative taken to plot the EEDF, such that the experimental result appears to deviate from the chi-squared form of the theoretical curve. The apparent deviation could be a real physical effect, but

may also be attributable to distortion of the spectrum near the inflection point induced by the notch filter.

The lower panel of figure 8 shows the same information as the top panel, but represented differently, showing the natural logarithm of the intensity versus the energy. Such a representation is frequently used in the literature. The red crosses and the green curve show the same data as for the top panel; the blue crosses correspond to the raw (unsmoothed) experimental data. In this representation, the theoretical and experimental data superpose, showing a linear variation characteristic of a Maxwellian distribution of electron velocities. The tail of the distribution near 2.5 eV deviates from the linear variation, but only because the signal approaches the noise level and this is associated with increased error in the smoothing algorithm. An interpretation based on this bottom panel figure would suggest that (i) the smoothing applied to produce the red crosses does not distort the raw data (blue crosses), and (ii) the data does not deviate from a Maxwellian distribution of electron velocities.

We interpret our data as potentially consistent with a Maxwellian distribution of electron velocities, but with the following caveats. In the top panel view, any deviations from a Maxwellian velocity distribution would be easily visible, however, so would any minor distortions unrelated to real deviations from Maxwellian behavior (such as imprecisions in the fit quality to the data). On the other hand, the bottom panel view, while appearing to reveal a Maxwellian distribution, can show only truly marked deviations from Maxwellian behavior (due to the logarithmic vertical scale). Some apparent deviation from Maxwellian behavior has been observed for a magnetized version of the hollow cathode plasma source studied with Langmuir probes [57].

4.4. Measurement uncertainties

The uncertainties associated with the measurement of the n_e and T_e are due to a number of factors. The laser power (rms value) has been continuously monitored and fluctuates by a maximum value of 1% over the 10 min acquisition duration of the experiments. We have specifically chosen a capacitive diaphragm pressure gauge (Inficon CDG025D, temperature compensated) with high precision in the region of pressures at which we perform our Raman calibrations. The precision of this gauge in the range of 1.3×10^{-3}–13.3 mbar is 0.2%.

There is an uncertainty due to the quality of the Gaussian fit to the experimental data and this is computed by extracting the covariance matrix at the time of fitting. This uncertainty depends on the signal to noise ratio and can be significant for low-amplitude scattered signals. The largest source of uncertainty for large-amplitude scattered signals is, however, due to the uncertainty in the value of the Raman cross-sections used for fitting; this is 8% [47].

4.5. Plasma perturbation and the detection limit

To check plasma disturbance, we can apply the form described in the work of Carbone and Nijdam [37] for the critical laser fluence for perturbation,

$$F_{\mathrm{crit}} = \frac{6\pi^2 m_e \epsilon_0 c^3 k_{\mathrm{B}} T_e}{e^2 \nu_{eh} \lambda^2} \xi, \tag{12}$$

where m_e is the electron mass, ϵ_0 the vacuum permittivity, c the speed of light in a vacuum, and k_{B} Boltzmann's constant. The electronic charge is denoted by e and the laser wavelength by λ. ξ is defined as an arbitrary acceptable ratio of temperature perturbation ΔT_e to the electron temperature T_e.

This form contains a total collision frequency term ν_{eh} for electrons with heavy species. ν_{eh} is the sum of the electron–ion collision frequency ν_{ei} and the electron-neutral collision frequency ν_{en}.

Using the forms given in Froula [36], $\nu_{\mathrm{ei}} = 2.92 \times 10^{-6} n_i[\mathrm{cm}^{-3}] \cdot (T_e[\mathrm{eV}])^{-3/2} \ln\Lambda \ \ \mathrm{s}^{-1}$, where $\Lambda = 1.53 \times 10^{10} (T_e[\mathrm{eV}])^{3/2} / (n_e[\mathrm{cm}^{-3}])^{1/2}$, and $\nu_{\mathrm{en}} = 2.8 \times 10^8 (r_n[\mathrm{cm}])^2 n_n[\mathrm{cm}^{-3}] (T_e[\mathrm{eV}])^{1/2} \ \mathrm{s}^{-1}$. In these forms n_i, n_e and n_n are the ion, electron and neutral densities, respectively. r_n is the effective radius of the neutral.

To apply these forms, we use a 'worst case scenario' which would give the lowest value of F_{crit} applicable to our plasma. We assume an upper limit on T_e of 10 eV, an upper limit on n_e and n_i of 10^{13} cm^{-3} and an upper limit of 10^{15} cm^{-3} for n_n. This gives a value of Λ of 1.53×10^5 eV cm^{-3}. The corresponding value of ν_{ei} is 1.10×10^7 s^{-1}. The value of ν_{en} is 8.85×10^7 s^{-1}, giving a value of ν_{eh} of 9.95×10^7 s^{-1}.

For equation (12), we assign an acceptable value of ξ of 0.01. Substituting in the other parameters (maintaining T_e of 10 eV and using the calculated value of ν_{eh}, we obtain a value of F_{crit} of 2.86×10^7 J m^{-2}.

Now, for our experiment, with a peak value of laser pulse energy of 430 mJ and a beam diameter in the observation region of 0.3 mm, we obtain a fluence F_{exp} of 6.08×10^6 J m^{-2}. This value of F_{exp} is well below the threshold value F_{crit} for disturbing the plasma.

As recently established by Shneider [18], ponderomotive forces on the electrons could result in density perturbations for a low temperature, low density plasma, affecting the measurement accuracy. The relative density perturbation is given by [18]

$$\frac{|\delta n|}{n_e} = \frac{e^2 I_0}{\bar{e} m_e \omega^2 \epsilon_0 c k_{\mathrm{B}} T_e (1 + 0.5 r_L^2 / r_{\mathrm{D}}^2)}, \tag{13}$$

where I_0 is the laser intensity used, $\bar{e}$ is Euler's constant, ω is the laser radiation angular frequency, given by $2\pi c/\lambda$, r_L is the beam waist radius and r_{D} the Debye length.

To check the largest possible density perturbation in our case, we assume a lower limit on density and a lower limit on electron temperature, respectively 10^{14} m^{-3} and 0.1 eV. This combination gives 2.35×10^{-4} m for r_{D}; r_L is 1.5×10^{-4} m. The corresponding relative density perturbation obtained from equation (13) is 1.6%; even considering this extreme case, the density perturbation is negligible. For any higher T_e and n_e, the relative perturbation would be lower.

Finally, we briefly consider possible photoionization of metastable atoms: this issue has been examined for a xenon microwave plasma by Yamamoto and colleagues [58].

In their work, a threshold incident laser intensity of 1×10^{15} W m^{-2} was established empirically for photo-ionization of xenon metastables. The value we obtain for our incident intensity is 1.01×10^{15} W m^{-2}, close to the threshold of Yamamoto. However, we have no means of knowing whether the two plasmas are truly comparable, and the proportion of metastables present is unknown for both.

Overall, after consideration of the main possible effects (plasma heating, ponderomotive force contributions), it appears that we can neglect plasma perturbations in our implementation.

Regarding the detection limit, we have established in this work a detection limit of 10^{16} m^{-3}. This limit is determined not only by the characteristics of our transmission and detection branches, but also by the type of plasma under study. For electronegative plasmas, it would be necessary to reduce the laser fluence to avoid photodetachment of electrons. This would be an issue if the incident photon energy (2.43 eV for 532 nm) exceeds the electron attachment energy for a given species. Reducing the laser energy to prevent photodetachment would result in fewer scattered photons for the scattered spectrum, raising the detection limit above 10^{16} m^{-3} (unless this is compensated for, for example, by increasing the number of laser shots or the detection sensitivity). Our detection limit is also expected to be higher in atmospheric pressure plasmas; in such environments, van Gessel [45] identified a detection limit of about 5×10^{18} m^{-3}, due to the influence of strong plasma emission and Rayleigh scattering.

4.6. Planned diagnostic upgrades

Additional options exist for lowering the detection limit, and these adaptations will be implemented over the next few months. The first is the use of a camera equipped with a Gen III intensifier with a higher quantum efficiency (50% at 532 nm) and a back-illuminated ICCD to improve sensitivity. The use of a detector based on recently-developed emICCD technology is another option, and would allow for single photon detection while preserving the subnanosecond exposure times available with a gated ICCD. The high linearity of response of these detectors over a large range of signal intensities, in comparison to standard ICCDs, would also guarantee even higher reliability of calibrations.

Another planned upgrade is the use of a larger VBG notch filter; in the current setup, fully half of the collected power arriving at the filter is not transmitted to the spectrometer because it falls outside the filter dimensions. In addition, in future experimental implementations for which a large degree of stray light is expected (for example, close to material surfaces), the use of two stacked VBG notch filters to improve stray light attenuation is an option. Such an arrangement would still guarantee lower losses than a triple grating spectrometer.

5. Conclusions

A new compact ITS diagnostic known as THETIS has been designed, constructed and validated. This diagnostic uses a VBG notch filter for the first time in ITS studies, providing high stray light attenuation within a limited wavelength range around the incident laser line. The use of a VBG and a single spectrometer ensures diagnostic compactness and reduced transmission losses in comparison to assemblies using triple grating spectrometers. These features make THETIS a flexible, high-performance platform, suited to installation on a range of low-temperature laboratory plasma sources.

A hollow cathode, used as an electron source for Hall thrusters, is chosen for the first diagnostic tests. The diagnostic sensitivity gives access to electron density measurements down to the 10^{16} m^{-3} range; the narrowness of the VBG wavelength cutoff preserves access to measurements of electron temperatures below 1 eV.

Acknowledgments

The authors would like to express their gratitude to members of the SACM team of CEA/Saclay (J Schwindling and O Tuske). The contributions of G Largeau, L Peilleron and E Labrude, and advice from P Bernhard and H J van der Meiden, were also appreciated. The authors acknowledge support from the French Alternative Energies and Atomic Energy Commission (CEA) and the French Space Agency (CNES).

ORCID iDs

Benjamin Vincent https://orcid.org/0000-0001-5420-6002
Sedina Tsikata https://orcid.org/0000-0001-5104-0676

References

[1] Mott-Smith H M and Langmuir I 1926 *Phys. Rev.* **28** 727
[2] Kagan Y M and Perel' V I 1963 *Sov. Phys. Usp.* **81** 767
[3] Guthrie A and Wakerling R K 1949 *The Characteristics of Electrical Discharges in Magnetic Fields* (New York: McGraw-Hill)
[4] Arslanbekov R R, Khromov N A and Kudryavtsev A A 1994 *Plasma Sources Sci. Technol.* **3** 528
[5] Fantz U 2006 *Plasma Sources Sci. Technol.* **15** S137
[6] Donnelly V M 2004 *J. Phys. D: Appl. Phys.* **37** R217
[7] Turner R and Poehler T O 1968 *J. Appl. Phys.* **39** 5726
[8] Neumann G, Bänziger U, Kammeyer M and Lange M 1993 *Rev. Sci. Instrum.* **64** 19
[9] Griem H R 1997 *Principles of Plasma Spectroscopy* (Cambridge: Cambridge University Press)
[10] Bates D R, Kingston A E and McWhirter R W P 1962 *Proc. R. Soc.* A **267** 297
[11] Hutchinson I H 2001 *Principles of Plasma Diagnostics* (Cambridge: Cambridge University Press)
[12] Peacock N J, Robinson D C, Forrest M J, Wilcock P D and Sannikov V V 1969 *Nature* **224** 488

[13] Artsimovich L A *et al* 1969 *Plasma Physics and Controlled Fusion Research (IAEA)* p 157 CN24/B1
[14] Lasalle J and Platz P 1979 *Appl. Opt.* **18** 4124
[15] Pasqualotto R, Nielsen P, Gowers C, Beurskens M, Kempenaars M, Carlstrom T, Johnson D and J-E contributors 2004 *Rev. Sci. Instrum.* **75** 3891
[16] Kantor M Y, Donné A J H, Jaspers R, van der Meiden H J and T Team 2009 *Plasma Phys. Control. Fusion* **51** 055002
[17] Han X, Shao C, Xi X, Zhao J, Qing Z, Yang J, Dai X and Shinichiro K 2013 *Rev. Sci. Instrum.* **84** 053502
[18] Shneider M N 2017 *Phys. Plasmas* **24** 100701
[19] van de Sanden M C M, Janssen G M, de Regt J M, Schram D C, van der Mullen J A M and van der Sijde B 1992 *Rev. Sci. Instrum.* **63** 3369
[20] de Regt J M, Engeln R A H, de Groote F P J, van der Mullen J A M and Schram D C 1995 *Rev. Sci. Instrum.* **66** 3228
[21] Bowden M D, Goto Y, Yanaga H, Howarth P J A, Uchino K and Muraoka K 1999 *Plasma Sources Sci. Technol.* **8** 203
[22] Bowden M D, Kogano M, Suetome Y, Hori T, Uchino K and Muraoka K 1999 *J. Vac. Sci. Technol.* A **17** 493
[23] Crintea D L, Czarnetzki U, Iordanova S, Koleva I and Luggenhölscher D 2009 *J. Phys. D: Appl. Phys.* **42** 045208
[24] Carbone E A D, Hübner S, Palomares J M and van der Mullen J J A M 2012 *J. Phys. D: Appl. Phys.* **45** 345203
[25] Seo B H, You S J and Kim J H 2015 *Japan. J. Appl. Phys.* **54** 086102
[26] Zhurin V V, Kaufman H R and Robinson R S 1999 *Plasma Sources Sci. Technol.* **8** R1
[27] Csiky G A 1969 *AIAA 7th Electric Propulsion Conf. (Williamsburg, VA, 3–5 March)* 60-258
[28] Kelly P J and Arnell R D 2000 *Vacuum* **56** 159
[29] Tuske O, Adroit G, Delferrière O, Menezes D D, Gauthier Y, Gobin R and Harrault F 2008 *Rev. Sci. Instrum.* **79** 02B710
[30] Yamamoto N, Tomita K, Yamasaki N, Tsuru T, Ezaki T, Kotani Y, Uchino K and Nakashima H 2010 *Plasma Sources Sci. Technol.* **19** 045009
[31] Washeleski R L 2013 Laser Thomson scattering measurements of electron temperature and density in a Hall-effect plasma *PhD Thesis* Michigan Technological University, Michigan, USA
[32] Friss A and Yalin A 2017 *AIAA Propulsion and Energy Forum, 53rd AIAA/SAE/ASEE Joint Propulsion Conf. (Atlanta, GA, 10–12 July)* 2017-4792
[33] Tsikata S, Lemoine N, Pisarev V and Grésillon D 2009 *Phys. Plasmas* **16** 033506
[34] Cavalier J, Lemoine N, Bonhomme G, Tsikata S, Honoré C and Grésillon D 2013 *Phys. Plasmas* **20** 082107
[35] Gary S P and Sanderson J J 1970 *J. Plasma Phys.* **4** 739
[36] Froula D H, Glenzer S H, Luhmann N C Jr and Sheffield J 2011 *Plasma Scattering of Electromagnetic Radiation: Theory and Measurement Techniques* (New York: Academic)
[37] Carbone E and Nijdam S 2015 *Plasma Phys. Control. Fusion* **57** 014026
[38] van der Meiden H J *et al* 2008 *Rev. Sci. Instrum.* **79** 013505
[39] Paillet M, Meunier F, Verhaegen M, Blais-Ouellette S and Martel R 2010 *Rev. Sci. Instrum.* **81** 053111
[40] Klarenaar B L M, Brehmer F, Welzel S, van der Meiden H J, van de Sanden M C M and Engeln R 2015 *Rev. Sci. Instrum.* **86** 046106
[41] Palomares J M, Iordanova E I, Gamero A, Sola A and Mullen J J A M v d 2010 *J. Phys. D: Appl. Phys.* **43** 395202
[42] Muraoka K and Kono A 2011 *J. Phys. D: Appl. Phys.* **44** 043001
[43] Bakker L P, Freriks J M, de Hoog F J and Kroesen G M W 2000 *Rev. Sci. Instrum.* **71** 2007
[44] van de Sande M J, Deckers R H M, Lepkojus F, Buscher W and van der Mullen J J A M 2002 *Plasma Sources Sci. Technol.* **11** 466
[45] van Gessel A F H, Carbone E A D, Bruggeman P J and van der Mullen J J A M 2012 *Plasma Sources Sci. Technol.* **21** 015003
[46] Bernath P F 2005 *Spectra of Atoms and Molecules* (Oxford: Oxford University Press)
[47] Penney C M, Peters R L S and Lapp M 1973 *J. Opt. Soc. Am.* **64** 712
[48] Goebel D M, Watkins R M and Jameson K K 2007 *J. Propul. Power* **23** 552
[49] Sary G 2016 Modélisation d'une cathode creuse pour propulseur à plasma *PhD Thesis* Université de Toulouse 3 Paul Sabatier, Toulouse, France
[50] Nürmberger F, Hock A and Tajmar M 2015 *AIAA 7th Propulsion and Energy Forum, 51st AIAA/SAE/ASEE Joint Propulsion Conf. (Orlando, FL, 27–29 July)* 2015-3822
[51] Goebel D M and Chu E 2011 *32nd Int. Electric Propulsion Conf. (Wiesbaden, 11–15 September)* 2011-053
[52] Bugrova A I, Kim V, Maslennikov N A and Morozov A I 1991 *22nd Int. Electric Propulsion Conf. (Viareggio, Italy, 14–17 October)* 1991-079
[53] Dannenmayer K, Kudrna P, Tichý M and Mazouffre S 2012 *Plasma Sources Sci. Technol.* **21** 055020
[54] Hori T, Kogano M, Bowden M D, Uchino K and Muraoka K 1998 *J. Appl. Phys.* **83** 1909
[55] Kono A and Funahashi H 2002 *J. Appl. Phys.* **92** 1757
[56] Huang M, Warner K, Lehn S and Hieftje G M 2000 *Spectrochim. Acta* B **55** 1397
[57] Avaria G, Lunk A, Schröeder A and Vinogradov I P 2009 *Plasma Process. Polym.* **6** S352
[58] Yamamoto N, Tomita K, Sugita K, Kurita T, Nakashima H and Uchino K 2012 *Rev. Sci. Instrum.* **83** 073106